Rapid Communications

Covalency driven modulation of paramagnetism and development of lone pair ferroelectricity in multiferroic $Pb_3TeMn_3P_2O_{14}$

Rafikul Ali Saha,[1] Anita Halder,[2] Tanusri Saha-Dasgupta,[2] Desheng Fu,[3] Mitsuru Itoh,[4] and Sugata Ray[1,*]

[1]*School of Materials Sciences, Indian Association for the Cultivation of Science, 2A & 2B Raja S. C. Mullick Road, Jadavpur, Kolkata 700032, India*

[2]*Department of Condensed Matter Physics and Material Sciences, S. N. Bose National Centre for Basic Sciences, Block JD, Sector 3, Saltlake, Kolkata 700106, India*

[3]*Department of Electronics and Materials Science, and Department of Optoelectronics and Nanostructure Science, Graduate School of Science and Technology, Shizuoka University, 3-5-1 Johoku, Naka-ku, Hamamatsu 432-8561, Japan*

[4]*Materials and Structures Laboratory, Tokyo Institute of Technology, 4259 Nagatsuta, Yokohama 226-8503, Japan*

(Received 1 January 2020; revised manuscript received 5 March 2020; accepted 4 May 2020; published 20 May 2020)

We have investigated the structural, magnetic, and dielectric properties of the Pb-based langasite compound $Pb_3TeMn_3P_2O_{14}$ both experimentally and theoretically in light of metal-oxygen covalency, and the consequent generation of multiferroicity. It is known that the large covalency between Pb 6*p* and O 2*p* plays an instrumental role behind the stereochemical lone pair activity of Pb. The same happens here, but a subtle structural phase transition above room temperature changes the degree of such lone pair activity and the system becomes ferroelectric below 310 K. Interestingly, this structural change also modulates the charge densities on different constituent atoms and consequently the overall magnetic response of the system while maintaining the global paramagnetism behavior of the compound. This single origin of modulation in polarity and paramagnetism inherently connects both functionalities and the system exhibits mutiferroicity at room temperature.

DOI: 10.1103/PhysRevB.101.180406

Introduction. The story of stereochemically active cationic lone pairs, arising due to *s*-*p* mixing in a metal assisted by covalency with the ligand *p* orbitals and finally driving ferroelectricity within a polar unit cell, has always been an exciting point of discussion in condensed matter physics [1]. There is a sizable number of systems where this mechanism plausibly works, such as ferroelectric perovskites ($PbTiO_3$, $BiMnO_3$, $BiFeO_3$, $SnTiO_3$, $CsPbF_3$, etc.) [2–7], double perovskites ($Pb_2ScTi_{0.5}Te_{0.5}O_6$, $Pb_2ScSc_{0.33}Te_{0.66}O_6$, Pb_2MnWO_6) [8,9], as well as α-PbO [10], SnO, BiOF [11], Bi_2WO_6 [12], $BiMn_2O_5$ [13], etc. Among these, systems which also accommodate magnetic cations and the consequent possibility of multiferroicity draw much enhanced attention. The two most prominent examples of such multiferroics having significant roles of lone pair and covalency are $BiFeO_3$ [5,14] and $BiMnO_3$ [4,15]. Among these, $BiFeO_3$ undergoes a ferroelectric phase transition with $T_C = 1100$ K [16] and a *G*-type antiferromagnetic transition at a lower temperature (650 K), accompanied by an incommensurate spin cycloid structure having a period of 620 Å [17,18]. Due to this incommensurate spatially modulated cycloid spin structure, a linear magnetoelectric (ME) effect is not observed in $BiFeO_3$, however, the polarization breaks the crystal symmetry and manifests itself in the appearance of an inhomogeneous ME interaction (Lifshitz invariant), showing a quadratic dependence of polarization on the magnetic field [19]. On the other hand, $BiMnO_3$ is one of the very few multiferroics that is ferroelectric (~770 K) and ferromagnetic ($T_C = 105$ K) [20–22]. In this case the ferroelectricity has been explained by the presence of a stereochemically active Bi^{3+} $6s^2$ lone pair, developing from the mixing of the Bi 6*s* and 6*p* orbitals, activated by charge transfer from a fully filled anionic orbital to an empty Bi 6*p* orbital. As a result, the system becomes structurally noncentrosymmetric below 770 K [23] and a distinct magnetoelectric response of −0.6% is observed at the magnetic transition temperature [23].

In this context we have explored the rarely studied langasites ($A_3BC_3D_2O_{14}$), having lone pair bearing Pb^{2+} ions and 3*d* transition metal (TM) ions within TMO_4 tetrahedral units. Tetrahedral coordinations are traditionally more conducive for a TM-O covalent interaction [24–27], which plays a crucial role in deciding the degree of lone pair activity of Pb by manipulating the available electron density on the oxygen, sharing both TM and Pb connections. In the family of langasites, *C* and *D* site cations remain in tetrahedral coordination, while *B* and *A* sites form octahedral and decahedral networks, respectively [28–33]. The network of *A* cations forms a topologically equivalent kagome lattice from well-separated planes of corner-sharing triangles [34]. Members of the langasite family are known to host multiferroism, nonlinear optical, piezoelectric, ferroelectric, and dielectric properties [29], e.g., Fe-based langasite compounds $A_3BFe_3D_2O_{14}$ (A = Ba, Sr, Ca; B = Ta, Nb, Sb; D = Ge, Si) show frustration driven helical magnetic order, accompanied by a dielectric anomaly at the onset of a magnetic transition [28,35].

*mssr@iacs.res.in

However, lone pair driven multiferroicity in langasites has yet to be explored.

$Pb_3TeMn_3P_2O_{14}$ (PTMPO) can become important exactly in this context where changes in the degree of stereochemical lone pair activity of Pb^{2+} distorts the general nonpolar structure into a polar one, causing a shifting of magnetic Mn/P planes (M-P planes) towards the neighboring Pb/Te containing planes (P-T plane) in the direction of a positive c axis. This results in the formation of a stripelike distribution of pairwise closely placed M-P/P-T planes within the structure which in turn enhances the covalency as well as magnetic moments on otherwise nonmagnetic entities such as Pb^{2+}, Te^{6+}, P^{5+}, and O^{2-}. This structural change brings forth spontaneous polarization in the system at around ∼310 K, and the synchronous redistribution of magnetic moments on the ions and shortened relative distances among them affect the overall paramagnetic state, which gets manifested in a clear signal of magnetoelectric coupling within the apparent paramagnetic phase, i.e., far above the long-range magnetic transition (∼7 K) of the system. Such unusual phenomena have been reported recently [36,37] in spin-chain compounds and have been explained by the variations of short-range magnetic correlations within the paramagnetic phase.

Overall, in this Rapid Communication we present a different multiferroic with room-temperature magnetoelectric coupling arising from covalency affected stereochemical activity of a lone pair and coincident changes in the local magnetic correlations.

Experimental and theoretical details are elaborately presented in the Supplemental Material [38].

Structure from x-ray diffraction. The structural refinement of room-temperature x-ray diffraction (XRD) of PTMPO has been performed by considering the noncentrosymmetric and polar trigonal space group ($P3$) (the lattice parameter and crystal structure are given in Tables S1 and S2 of the Supplemental Material [38]), consistent with previous literature reports [29,39]. Temperature-dependent x-ray diffractions have been collected over a wide temperature range of 5–400 K. The Rietveld refinements [38] of these collected XRD patterns have been carried out using the same trigonal space group $P3$. Thermal variations of the refined lattice parameters, a, b, c and unit cell volume are shown in Figs. 1(a)–1(c). Two anomalies at ∼310 and ∼120 K are observed in the temperature-dependent lattice parameters as well as unit cell volume variations. We performed the 299-K XRD refinement using both $P321$ and $P3$ space groups, as shown in Figs. S1(a) and S1(b) of the Supplemental Material [38], respectively. It is clearly evident from the fitting that the higher-symmetry $P321$ space group could not capture the superlattice peaks in the low-temperature diffraction pattern [blue ellipse line in Fig. S1(a) of the Supplemental Material [38]]. On the other hand, the superlattice peaks have been well reproduced while fitting using the low-symmetry $P3$ space group [as indicated in Fig. S1(b) of the Supplemental Material [38]]. Most importantly, the room-temperature synchrotron data also are very similar to our laboratory XRD results, as shown in Figs. S1(d)–S1(f) of the Supplemental Material [38]. This convincingly affirms the room-temperature ferroelectric phase ($P3$) for the studied sample. It is important to note that the absence of superlattice peaks in the 400-K XRD refinement [see Fig. S1(c) of the Supplemental Material [38]] signifies the higher-symmetric structure (space group $P321$) of the sample above 310 K which is noncentrosymmetric and nonpolar. Therefore, it can be concluded that above 310 K, the system has a nonpolar $P321$ structure (see Tables S1 and S3 of the Supplemental Material [38]), but the symmetry gets lifted (polar $P3$) with cooling and the polar structure only gets further distorted below 120 K.

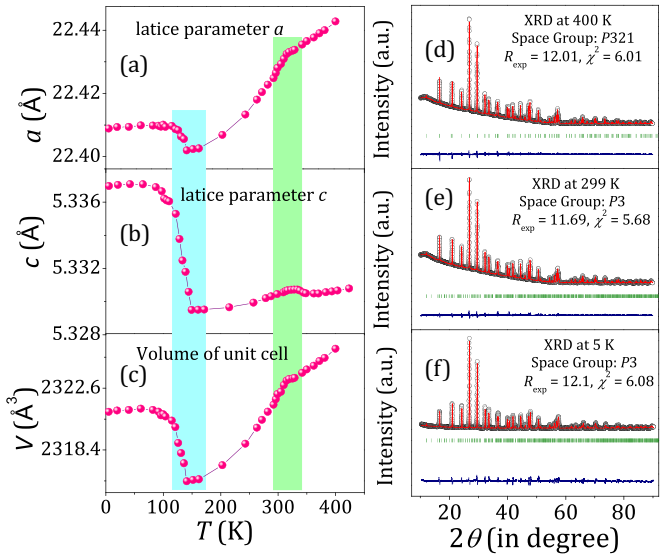

FIG. 1. (a)–(c) Thermal variation of lattice parameters and volume of unit cell of PTMPO. (d)–(f) are the refined XRD patterns of 400, 299, and 5 K data, respectively. Open black circles represent the experimental data and the continuous red line represents the calculated pattern. The blue line represents the difference between the observed and calculated pattern. The green scattered lines are the Bragg peak.

Due to this structural phase transition ($P321$ to $P3$), the unit cell becomes larger and all Pb and Mn equilateral triangles get converted to scalene triangles [see Fig. S1(g) of the Supplemental Material [38]]. The lower-symmetry $P3$ space group is a subgroup of $P321$, and is achieved by removing the C_2 symmetry from $P321$. This happens when the M-P plane is shifted towards the P-T plane in the direction of the positive c axis [Figs. 2(a) and 2(b)]. As a result, the Mn-O bond lengths become shorter, ensuring a larger covalent interaction (see Table I) and a plausible enhancement of the stereochemical activity of the Pb^{2+} lone pair. This shift also affects the overall site symmetry as all the Pb and Mn triangles become scalene, as shown in Figs. 2(c) and 2(d). This unit cell with lower symmetry becomes large, containing seven formula units per unit cell.

Interestingly, these scalene triangles of Pb, Mn, and Te are found to be connected through systematic 120° rotations (see Figs. S2 and S3 of the Supplemental Material [38]) and it may be anticipated that a stereochemically active Pb^{2+} ($6s^2$) lone pair is responsible for such deformations of the structural motifs.

However, it is primarily important to confirm the existence of a stereochemically active Pb^{2+} lone pair at all temperatures, while the degree may change with structural transitions. If

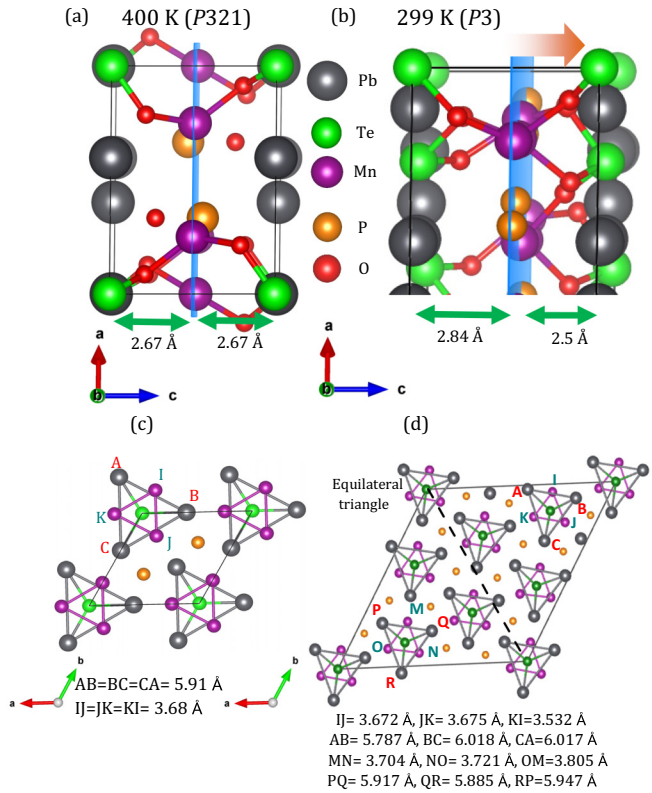

FIG. 2. (a) and (b) are the *a*-*c* plane of the *P*321 and *P*3 structures, respectively. (c) and (d) *a*-*b* plane of the *P*321 and *P*3 structures, respectively.

we divide the Pb-O polyhedron into two spheres (I and II), the difference between the shortest Pb-O distances of the two spheres ($\triangle E_1$) provides a measure of the asymmetry, degree of delocalization, and lone pair activity. The other notable parameter in this regard is $\triangle E_2$, which is the difference between the shortest Pb-O distance in the polyhedron of PTMPO and the known shortest Pb-O distance in compounds containing these elements. A large value of $\triangle E_1$ and smaller value of $\triangle E_2$ attribute higher stereochemical activity to the ns^2 lone pair [5]. Here, to estimate $\triangle E_2$, we considered the minimal distance $d_{Pb^{2+}\text{-}O}$ (2.40 Å) from $Pb_2V_5O_{12}$ [5]. Thus the values of $\triangle E_1$ turn out to be 0.44 and 0.36 Å while $\triangle E_2$ are −0.04 and 0.06 Å for *P*3 and *P*321 space groups, respectively, indicating a higher degree of stereochemical activity of the Pb^{2+} lone pair in the *P*3 structure of PTMPO, which is in line with the existing results of $BiFeO_3$ compounds [5].

Theoretical calculations. We have carried out density functional theory (DFT) [38] calculations in order to assess the covalency effect which is important for the stereochemical activity of the Pb lone pair. Since the goal of our first-principles calculation is to reveal the covalency effect between different cations and oxygen and the effect of the structural transition on it, the analysis of the electron structure was carried out on spin-polarized calculations. The antiferromagnetic structure, which is the ground-state magnetic structure, is complex and leads to the cancellation of the covalency effect due to the opposite alignment of spins, as ascertained in the vanishing moment of oxygen compared to its finite value in the fully spin-polarized calculation (see Table II). The calculations have been carried out both for nonpolar (high-temperature *P*321) and polar (low-temperature *P*3) structures and the detailed density of states (DOS) is shown in Figs. 3(a) and 3(d), respectively. The stereochemical activity of lone pair active ions such as Bi^{3+} or Pb^{2+} within oxide structures has been argued to originate from the hybridization between 6*s*, 6*p* orbitals at the Bi/Pb site and 2*p* orbitals at the O site. The degree of stereochemical activity is thus crucially dependent on the energy level positions of these states, especially the position of 6*p*. The 6*p*-2*p* hybridization turns out to be the governing factor in giving rise to directionality of the lone pair and driving the off-centric movement [1]. Comparing between the projected DOS of PTMPO at high-temperature nonpolar (*P*321) and low-temperature polar (*P*3) phases we observe a marked change in the position of Pb 6*p*, where it is closer to O 2*p* by about 1.5 eV in the low-temperature phase, compared to that in the high-temperature phase, suggestive of an enhanced interaction between Pb 6*s*-O 2*p* antibonding orbitals with the empty Pb 6*p* orbital [1]. This has been quantitatively confirmed from our crystal orbital Hamilton population (COHP) [38] calculation where the integrated COHP (ICOHP) values have been found to become double for the Pb-O connectivity while going from the *P*321 to *P*3 structure (see Fig. S4 and Table S4 in the Supplemental Material [38]). Such an effect should obviously enhance the degree of Pb lone pair activity in the compound at lower temperature. Interestingly, in the langasite structures, this also affects the energy position of the orbitals and electron density on Te because Pb and Te share a common oxygen. This effect is clearly reflected in the projected DOS, which shows Te 5*p* to be closer to oxygen 2*p* by 1 eV in the low-temperature phase compared to that in the high-temperature phase. As a result of this, there evolves an off-centric movement of an otherwise nominally Te^{6+} ion

TABLE II. Magnetic moment of PTMPO compounds in μ_B.

Space group	Mn	Pb	Te	P	O
*P*321	4.632	0.008	0.034	0.009	0.021
*P*3	4.602	0.012	0.038	0.013	0.023

TABLE I. Bond lengths of *P*321 and *P*3 structures.

Bond length (Å) (*P*321 space group)	Bond length of longer site (Å) (*P*3 space group)	Bond length of shorter site (Å) (*P*3 space group)
Mn-O = 2.01	Mn-O = 2.11	Mn-O = 1.91
O-Pb = 2.35	O-Pb = 2.46	O-Pb = 2.33
O-Te = 1.93	O-Te = 1.97	O-Te = 1.83

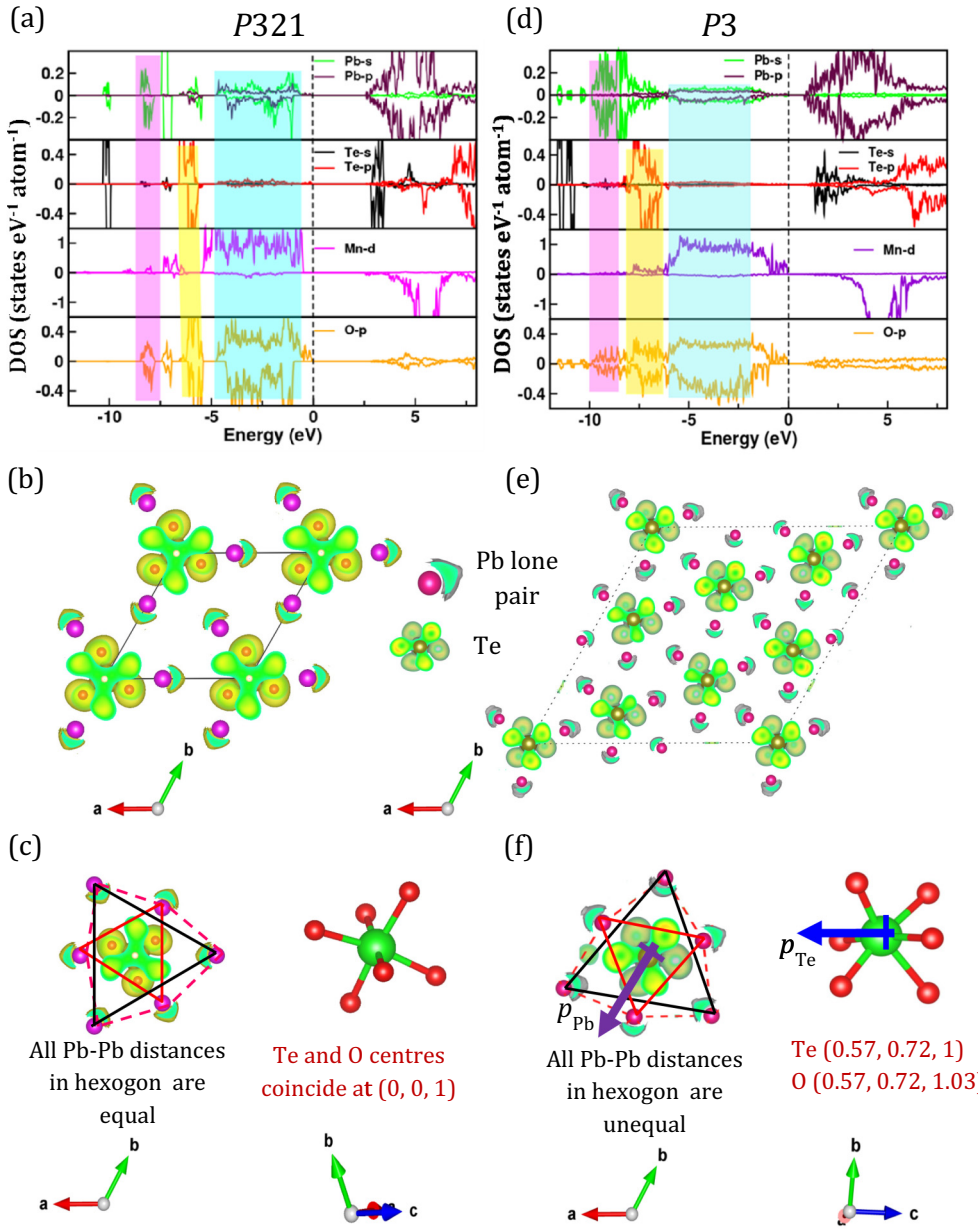

FIG. 3. (a)–(c) Partial DOS, electron localization function within a unit cell (the isosurfaces are visualized for a value of 0.3), and Pb_6 hexagon and TeO_6 octahedra of the $P321$ structure of PTMPO, respectively. (d)–(f) Partial DOS, electron localization function within a unit cell (the isosurfaces are visualized for a value of 0.3), and Pb_6 hexagon and TeO_6 octahedra of the $P321$ structure, respectively.

with two well-defined coordination shells of neighboring oxygen atoms in the low-temperature phase [see Fig. 3(f)], while at high temperature the off-centric movement of Te vanishes with only one coordination shell of neighboring oxygen atoms [see Fig. 3(c)]. Thus, clearly, dipoles are created within the system.

On top of it, the elemental magnetic moment possesses a noticeable change in the polar structure relative to the high-temperature nonpolar structure, in line with the stronger covalency effect of the polar structure (see Table II). The charge density distribution in the two structures indicates that there could be one more dipole moment center that might be created in the polar structure ($P3$) other than the polar geometry of TeO_6 octahedra. The stereochemically active lone pairs of Pb^{2+} (ns^2) in a Pb-Pb hexagon do not show any net polarization due to the equal length of the Pb-Pb distance in the $P321$ phase, as shown in Fig. 3(c), while in the polar structure, the Pb_6 hexagon creates a net dipole moment along the negative b direction with respect to the center of mass, as shown in Fig. 3(f). As the Pb_6 hexagon and TeO_6 octahedra possess dipole moments along the negative b and negative c directions, respectively, a net dipole moment within a single Pb_6 motif (where Te and Pb are present in the a-b plane) is generated along the b-c plane.

Dielectric measurements. All the results shown above are indicative of realizing a ferroelectric phase at room temperature in PTMPO, which is next checked by dielectric measurements. The temperature dependences of the real part

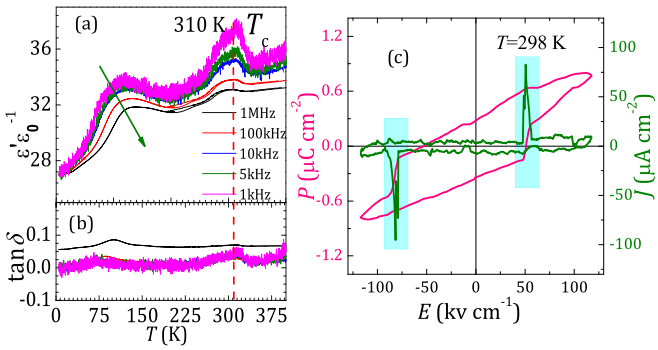

FIG. 4. (a) and (b) Temperature dependence of the real part of dielectric constant $\varepsilon'/\varepsilon_0$ and $\tan\delta$ loss data of PTMPO at different frequencies. (c) Electric-field-dependent polarization (pink line) and switching current behavior (green line)of PTMPO at room temperature.

of the dielectric constant ($\varepsilon'/\varepsilon_0$) and dielectric loss ($\tan\delta$) at different frequencies (1 kHz–1 MHz) in the temperature range of 5–400 K are shown in Figs. 4(a) and 4(b). A glasslike phase transition (frequency dependent) near 120 K and another frequency-independent anomaly near 315 K appear in the data. Clearly, the anomaly near 315 K appears due to the structural phase transition from the high-temperature nonpolar phase $P321$ to the low-temperature polar phase $P3$. Further, the polarization (P) with a varying electric field (E) at room temperature (298 K) has been measured, as indicated in Fig. 4(c), where a clear P-E loop with saturation and remnant polarization of 0.83 and 0.3 μC/cm^2, respectively, are observed at room temperature. Such a square loop along with sharp peaks in the switching current density (J) versus electric field (E) curve at room temperature [Fig. 4(c), light cyan shaded region] clearly confirm the existence of ferroelectric ordering in the sample at room temperature.

Magnetism, heat capacity, and magnetodielectric. Next, we focus on the magnetic properties of the compound. Zero-field-cooled (ZFC), field-cooled-cooling (FCC), and field-cooled-heating (FCH) magnetizations at 500, 5000, and 10 000 Oe were measured in the temperature range of 2–400 K, as shown in Fig. 5(a). A clear antiferromagnetic transition around $T_N =$ 7 K is observed in all the ZFC, FCC, and FCH curves, consistent with previous studies [29,30].

Interestingly, an unexpected effect is seen in the magnetic susceptibility at high temperature around the nonpolar to polar structural phase transition. A wide and thin hysteresis between the FCC and FCH data is observed around room temperature along with a distinct feature in the FCH curve [Fig. 5(b)]. Such behavior is reminiscent of a first-order phase transition which is unusual for a purely paramagnetic state. In order to reconfirm, we have repeatedly measured the M-T data of different batches of samples in different instruments and obtained the same result, confirming the robustness of the observation. It has been discussed earlier that the shift of the M-P plane towards the P-T plane at the phase transition affects the local covalency, effective moments on all the atoms (see Tables I and II), and probably the local magnetic correlations as well. It is likely that the local magnetic interaction gets affected quite substantially even though the system continues

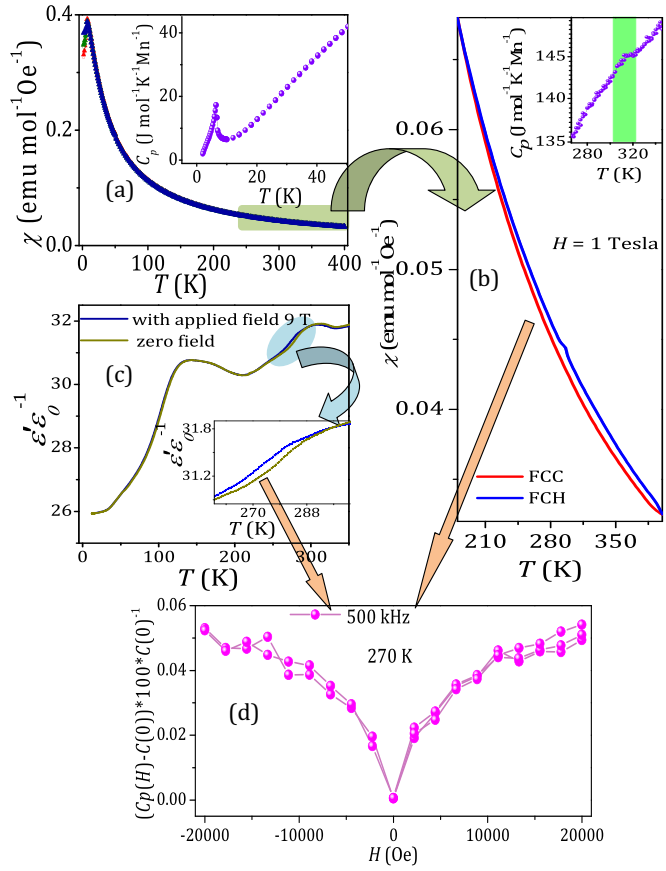

FIG. 5. (a) M-T at 500, 5000, and 10 000 Oe of PTMPO. Open red, solid red triangle, and solid red circle represent the ZFC, FCC, and FCH of 500 Oe data. Open green, solid green triangle, and solid green circle represent the ZFC, FCC, and FCH of 5000 Oe data. Open blue, solid blue triangle, and solid blue circle represent the ZFC, FCC, and FCH of 10 000 Oe data. The inset of (a) shows the heat capacity data at low temperature. (b) The red curve and blue curve are the FCC and FCH at 10 000 Oe data. The inset of (b) shows the heat capacity data at high temperature. (c) Temperature-dependent dielectric constant with zero field and 9-T field and the inset indicates the gap between them. (d) Magnetodielectric data at 270 K.

to remain a paramagnet globally. We tend to express the two different paramagnetic phases as PM-II (polar phase) and PM-I (nonpolar phase) which must be differing at the local scale as indicated by the susceptibility data. These features in magnetic susceptibility are further characterized by the zero-field heat capacity measurements (C_p vs T). A sharp λ-like anomaly, authentication mark of a thermodynamic phase transition into a long-range magnetic ordering has been observed near 7 K in the C_p vs T data [shown in the inset of Fig. 5(a)] which is in agreement with the magnetic susceptibility data. Interestingly, we observe an anomaly just above room temperature [see the inset of Fig. 5(b)], which maps the high-temperature magnetic anomaly (bifurcation in FCC and FCH) and the structural phase transition.

Further, we study the temperature-dependent dielectric constant under a 9-T magnetic field, shown in Fig. 5(c) along with the zero-field data. A significant change is observed between the with field data ($H = 9$ T) and without

field data near 270 K, as indicated in the inset to Fig. 5(c), signifying the presence of magnetoelectric coupling in the system. This magnetoelectric coupling is further established from the isothermal magnetoelectric data at 270 K, as shown in Fig. 5(d). Further, there is no significant change in magnetocapacitance with varying magnetic field at 315 K (see Fig. S5 of the Supplemental Material [38]), signifying the absence of magnetoelectric coupling above the ferroelectric phase transition. It can be argued that the structural phase transition brings forth ferroelectricity in the system below 310 K as a result of enhanced covalency and lone pair activity which at the same time affects the magnetism locally (introduction of the PM-II phase) and ensures a definite coupling between the two as they originate from the same microscopic effect.

Conclusion. We have reported the results of experimental and theoretical studies on the Pb-based langasite compound PTMPO. A clear ferroelectric transition is developed near 310 K. Stronger Mn-O covalent interactions help to redistribute the charges among the other cation-oxygen bonds, which in turn induces crucial electronic changes, and consequently the individual elemental magnetic moment gets changed in the system. The Mn-O covalency eventually facilitates the lone pair activity within Pb, which further displaces the magnetic Mn motif in the system. As a result, the system shows a first-order structural phase transition from $P321$ to $P3$ symmetry. The presence of an extra anomaly in the temperature-dependent XRD and dielectric data (near 120 K) is indicative of a further structural disruption locally with decreasing temperature within the trigonal symmetric space group of PTMPO compound. The phase transition at 310 K also affects the distribution of moments on the involved atoms locally, and as a result a finite magnetoelectric coupling is observed near room temperature. Our result not only introduces another multiferroic system with magnetoelectric coupling near room temperature, but also indicates other mechanisms for the development of such functionalities.

Acknowledgments. R.A.S. thanks CSIR, India and IACS for supporting fellowship. S.R. thanks the Technical Research Center of IACS. S.R. also thanks the Department of Science and Technology (DST) (Project No. WTI/2K15/74), UGC-DAE Consortium for Research, Mumbai, India (Project No. CRS-M-286) for support. A.H. and T.S.D. acknowledge the computational support of the Thematic Unit of Excellence on Computational Materials Science, funded by Nano-mission of Department of Science.

[1] A. Walsh, D. J. Payne, R. G. Egdell, and G. W. Watson, Chem. Soc. Rev. **40**, 4455 (2011).
[2] X. He and K.-j. Jin, Phys. Rev. B **94**, 224107 (2016).
[3] N. A. Hill and K. M. Rabe, Phys. Rev. B **59**, 8759 (1999).
[4] R. Seshadri and N. A. Hill, Chem. Mater. **13**, 2892 (2001).
[5] L. M. Volkova and D. V. Marinin, J Supercond. Novel Magn. **24**, 2161 (2011).
[6] K. C. Pitike, W. D. Parker, L. Louis, and S. M. Nakhmanson, Phys. Rev. B **91**, 035112 (2015).
[7] E. H. Smith, N. A. Benedek, and C. J. Fennie, Inorg. Chem. **54**, 8536 (2015).
[8] S. A. Larregola, J. A. Alonso, M. Alguero, R. Jimenez, E. Suard, F. Porcher, and J. C. Pedregosa, Dalton Trans. **39**, 5159 (2010).
[9] S. A. Ivanov, A. A. Bush, A. I. Stash, K. E. Kamentsev, V. Ya. Shkuratov, Y. O. Kvashnin, C. Autieri, I. D. Marco, B. Sanyal, O. Eriksson, P. Nordblad, and R. Mathieu, Inorg. Chem. **55**, 2791 (2016).
[10] G. W. Watson, S. C. Parker, and G. Kresse, Phys. Rev. B **59**, 8481 (1999).
[11] R. Seshadri, Proc. Indian Acad. Sci. (Chem. Sci.) **113**, 487 (2001).
[12] C. E. Mohn, and S. Stølen, Phys. Rev. B **83**, 014103 (2011).
[13] D. K. Shukla, S. Mollah, R. Kumar, P. Thakur, K. H. Chae, W. K. Choi, and A. Banerjee, J. Appl. Phys. **104**, 033707 (2008).
[14] S. Lee, M. T. Fernandez-Diaz, H. Kimura, Y. Noda, D. T. Adroja, S. Lee, J. Park, V. Kiryukhin, S.-W. Cheong, M. Mostovoy, and J.-G. Park, Phys. Rev. B **88**, 060103(R) (2013).
[15] P. Baetting, R. Seshadri, and N. A. Spaldin, J. Am. Chem. Soc. **129**, 9854 (2007).
[16] R. T. Smith, G. D. Achenbach, R. Gerson, and W. J. James, J. Appl. Phys. **39**, 70 (1968).
[17] I. Sosnowska, T. Peterlin-Neumaier, and E. J. Steichele, J. Phys. C: Solid State Phys. **15**, 4835 (1982).
[18] R. Przenioslo, M. Regulski, and I. Sosnowska, J. Phys. Soc. Jpn. **75**, 084718 (2006).
[19] A. M. Kadomtseva, A. K. Zvezdin, Yu. F. Popov, A. P. Pyatakov, and G. P. Vorob'ev, JETP Lett. **79**, 571 (2004).
[20] M. De Luca, D. Preziosi, F. Chiarella, R. Di Capua, S. Gariglio, S. Lettieri, and M. Salluzzo, Appl. Phys. Lett. **103**, 062902 (2013).
[21] C. C. Chou, C. L. Huang, S. Mukherjee, Q. Y. Chen, H. Sakurai, A. A. Belik, E. Takayama-Muromachi, and H. D. Yang, Phys. Rev. B **80**, 184426 (2009).
[22] Z. H. Chi, H. Yang, S. M. Feng, F. Y. Li, R. C. Yu, and C. Q. Jin, J. Magn. Magn. Mater. **310**, e358 (2007).
[23] T. Kimura, S. Kawamoto, I. Yamada, M. Azuma, M. Takano, and Y. Tokura, Phys. Rev. B **67**, 180401(R) (2003).
[24] R. J. Armstrong, A. H. Morrish, and G. A. Sawatzky, Phys. Lett. **23**, 414 (1966).
[25] F.-D. Tsay and L. Helmholtz, J. Chem. Phys. **50**, 2642 (1969).
[26] S.-J. Lee and S. Lee, New J. Phys. **8**, 98 (2006).
[27] P. M. Woodword, H. Mizoguchi, Y.-I. Kim, and M. W. Stoltzfus, in *Metal Oxides: Chemistry and Applications*, edited by J. L. G. Fierro (Taylor and Francis, London, 2006).
[28] K. Marty, P. Bordet, V. Simonet, M. Loire, R. Ballou, C. Darie, J. Kljun, P. Bonville, O. Isnard, P. Lejay, B. Zawilski, and C. Simon, Phys. Rev. B **81**, 054416 (2010).
[29] J. W. Krizan, C. de la Cruz, N. H. Andersen, and R. J. Cava, J. Solid State Chem. **203**, 310 (2013).
[30] H. J. Silverstein, A. Z. Sharma, K. Cruz-Kan, H. D. Zhou, A. Huq, R. Flacau, and C. R. Wiebe, J. Solid State Chem. **204**, 102 (2013).
[31] H. J. Silverstein, A. Z. Sharma, A. J. Stoller, K. Cruz-Kan, R. Flacau, R. L. Donaberger, H. D. Zhou, P. Manuel, A. Huq,

A. I. Kolesnikov, and C. R. Wiebe, J. Phys.: Condens. Matter **25**, 246004 (2013).

[32] M. M. Markina, B. V. Mill, E. A. Zvereva, A. V. Ushakov, S. V. Streltsov, and A. N. Vasiliev, Phys. Rev. B **89**, 104409 (2014).

[33] M. M. Markina, B. V. Mill, Y. A. Ovchenkov, E. A. Zvereva, and A. N. Vasiliev, Phys. Chem. Miner. **43**, 51 (2016).

[34] P. Bordet, I. Gelard, K. Marty, A. Ibanez, J. Robert, V. Simonet, B. Canals, R. Ballou, and P. Lejay, J. Phys.: Condens. Matter **18**, 5147 (2006).

[35] K. Marty, V. Simonet, E. Ressouche, R. Ballou, P. Lejay, and P. Bordet, Phys. Rev. Lett. **101**, 247201 (2008).

[36] T. Basu, V. V. R. Kishore, S. Gohil, K. Singh, N. Mohapatra, S. Bhattacharjee, B. Gonde, N. P. Lalla, P. Mahadevan, S. Ghosh, and E. V. Sampathkumaran, Sci. Rep. **4**, 5636 (2014).

[37] T. Basu, K. K. Iyer, K. Singh, and E. V. Sampathkumaran, Sci. Rep. **3**, 3104 (2013).

[38] See Supplemental Material at http://link.aps.org/supplemental/10.1103/PhysRevB.101.180406 for experimental and theoretical methods, structural parameters obtained from Rietveld refinement of XRD at different temperatures, crystal orbital Hamilton population calculation, and magnetocapacitance measurements at 277 and 315 K.

[39] H. J. Silverstein, A. Huq, M. Lee, E. S. Choi, H. Zhou, and C. R. Wiebe, J. Solid State Chem. **221**, 216 (2015).